

XQR-30: Black Hole Masses and Accretion Rates of 42 $z \gtrsim 6$ Quasars

C. Mazzucchelli^{1*}, M. Bischetti², V. D’Odorico^{2,3,4}, C. Feruglio², J.-T. Schindler⁵, M. Onoue^{6,7}, E. Bañados⁸, G. D. Becker⁹, F. Bian¹⁰, S. Carniani³, R. Decarli¹¹, A.-C. Eilers^{12**}, E. P. Farina¹³, S. Gallerani³, S. Lai¹⁴, R. A. Meyer⁸, S. Rojas-Ruiz⁸, S. Satyavolu¹⁵, B. P. Venemans⁵, F. Wang¹⁶, J. Yang¹⁶, Y. Zhu⁹

¹Instituto de Estudios Astrofísicos, Facultad de Ingeniería y Ciencias, Universidad Diego Portales, Avenida Ejército Libertador 441, Santiago, Chile.

²INAF–Osservatorio Astronomico di Trieste, Via G.B. Tiepolo, 11, I-34143 Trieste, Italy

³Scuola Normale Superiore, P.zza dei Cavalieri 7, I-56126 Pisa, Italy

⁴IFPU–Institute for Fundamental Physics of the Universe, via Beirut 2, I-34151 Trieste, Italy

⁵Leiden Observatory, Leiden University, Niels Bohrweg 2, 2333 CA Leiden, Netherlands

⁶Kavli Institute for Astronomy and Astrophysics, Peking University, Beijing 100871, People’s Republic of China

⁷Kavli Institute for the Physics and Mathematics of the Universe (Kavli IPMU, WPI), The University of Tokyo, Chiba 277-8583, Japan

⁸Max Planck Institut für Astronomie, Königstuhl 17, D-69117, Heidelberg, Germany

⁹Department of Physics & Astronomy, University of California, Riverside, CA 92521, USA

¹⁰ESO, Vitacura Alonso de Córdova 3107, Vitacura, Casilla 19001, Santiago de Chile, Chile

¹¹INAF - Osservatorio di Astrofisica e Scienza dello Spazio di Bologna, Via Gobetti 93/3, I-40129 Bologna, Italy

¹²MIT Kavli Institute for Astrophysics and Space Research, 77 Massachusetts Avenue, Cambridge, 02139, Massachusetts, USA

¹³Gemini Observatory, NSF’s NOIRLab, 670 N A’ohoku Place, Hilo, Hawai’i 96720, USA

¹⁴Research School of Astronomy and Astrophysics, Australian National University, Canberra, ACT 2611, Australia

¹⁵Tata Institute of Fundamental Research, Homi Bhabha Road, Mumbai 400005, India

¹⁶Steward Observatory, University of Arizona, 933 N Cherry Avenue, Tucson, AZ 85721, USA

Received September 15, 1996; accepted March 16, 1997

ABSTRACT

We present bolometric luminosities, black hole masses and Eddington ratios for 42 luminous quasars at $z \gtrsim 6$ using high signal-to-noise ratio VLT/X-Shooter spectra, acquired in the enlarged ESO Large Programme *XQR-30*. In particular, we derive bolometric luminosities from the rest-frame 3000 Å luminosities using a bolometric correction from the literature, and the black hole masses by modelling the spectral regions around the C IV 1549 Å and the Mg II 2798 Å emission lines, with scaling relations calibrated in the local universe. We find that the black hole masses derived from both emission lines are in the same range, and the scatter of the measurements agrees with expectations from the scaling relations. The Mg II-derived masses are between $\sim(0.8-12) \times 10^9 M_\odot$, and the derived Eddington ratios are within $\sim 0.13-1.73$, with a mean (median) of 0.84 (0.72). By comparing the total sample of quasars at $z > 5.8$, from this work and from the literature, to a bolometric luminosity distribution-matched sample at $z \sim 1.5$, we find that quasars at high redshift host slightly less massive black holes which accrete slightly more rapidly than at lower- z , with a difference in the mean Eddington ratios of the two samples of ~ 0.27 , in agreement with recent literature work.

Key words. (galaxies:) quasars: supermassive black holes – (galaxies:) quasars: emission lines – galaxies: high-redshift

1. Introduction

Quasars are the most luminous, non transient sources in the universe, hence they can be observed at very early cosmic times, into the Epoch of Reionization at $z \gtrsim 6$ (within the first billion years of the universe; e.g. Jiang et al. 2015, 2016, Bañados et al. 2016, Reed et al. 2019, Matsuoka et al. 2019), up to $z \sim 7.5$ (e.g. Bañados et al. 2018, Yang et al. 2020, Wang et al. 2021; see Fan et al. 2022 for a recent review). They are already powered by supermassive black holes (SMBHs) in their centers ($M_{\text{BH}} > 10^8 M_\odot$ e.g. Jiang et al. 2007, Shen et al. 2019), challenging models of early black holes formation and growth (e.g., Inayoshi et al. 2020 and Volonteri et al. 2021 for

recent reviews), and already present evolved broad-line-regions (BLRs) with super-Solar metallicities (e.g. Kurk et al. 2007, Lai et al. 2022). In order to grow a billion-solar masses SMBH by $z \gtrsim 6$, models require either a “light” ($\sim 10^2 M_\odot$) SMBH seed undergoing rapid super-Eddington accretion episodes, or a “heavy” ($\sim 10^5 M_\odot$) seed, which could also grow sub-Eddington (e.g. Volonteri 2010). Current studies identify PopIII stars as main candidates of the progenitors of light seeds (e.g. Bond et al. 1984, Valiante et al. 2016), while direct collapse of large primordial, low metallicity gas clouds produce $\sim 10^{5-6} M_\odot$ seeds (e.g. Oh & Haiman 2002, Begelman et al. 2006 Ferrara et al. 2014). Alternatively, runaway collisions and stellar-dynamical interactions in dense primordial star clusters can form seeds with intermediate masses ($\sim 10^{3-4} M_\odot$; e.g. Devecchi & Volonteri 2009, Sakurai et al. 2017). Another possibility to grow the

* email: chiara.mazzucchelli@mail.udp.cl

** Pappalardo Fellow

observed black hole masses is a radiatively inefficient accretion scenario, which may allow for $100\times$ higher mass accretion rates while remaining sub-Eddington, although this would require a large fraction of obscured quasars at high- z (e.g. Davies et al. 2019). Constraints from observational studies of black hole masses and accretion rates of sources at $z \gtrsim 6$ are therefore fundamental to inform SMBHs' formation theories and models, and to position them in the context of their (co-)evolution with their host galaxies (e.g. Pensabene et al. 2020, Neeleman et al. 2021).

Currently, ~ 100 measurements of $z \gtrsim 5.8$ SMBH masses have been reported in the literature, based on ground-based NIR spectroscopic data with limited signal-to-noise ratios (SNR; e.g. Shen et al. 2019, Yang et al. 2021; see Fan et al. 2022 for a recent review). The backbone of such studies is the modelling of the region around the rest-frame UV Mg II 2798 Å emission line, which can be used to derive black hole masses and accretion rates once virial equilibrium is assumed and taking advantage of scaling relations calibrated in the local universe (e.g. Vestergaard & Osmer 2009). Another routinely used emission line to measure black hole masses is the C IV 1549 Å (e.g. Vestergaard & Peterson 2006), especially in cases in which the Mg II falls in or close to telluric absorption, even if one has to consider larger uncertainties due to intrinsic, non virial components of the C IV line, arising from winds/outflows (e.g. Coatman et al. 2017). Although some studies suggest that $z \gtrsim 6$ quasars accrete at a rate comparable to that of a luminosity distribution-matched sample of quasars at $z \sim 1 - 2$ (e.g. Mazzucchelli et al. 2017, Shen et al. 2019), others observe a slight increase in Eddington ratio as a function of redshift (e.g. Yang et al. 2021, Farina et al. 2022). One of the main drawbacks of literature work so far is the low SNR of the considered data, which may introduce biases in the properties derived by the spectral fitting (e.g. Denney et al. 2016), and could highly deteriorate the C IV or Mg II line modeling in case of strong absorption features.

In this paper, we present measurements of bolometric luminosities, black hole masses and accretion rates from the modeling of the Mg II and C IV emission line regions for a sample of 42 luminous $z \sim 6$ quasars from the enlarged XQR-30 survey (E-XQR-30). In particular, 30 objects were observed in the Legacy Survey of quasars at $z = 5.8 - 6.6$ XQR-30 (D'Odorico et al. 2023; in this paper also referred to as “XQR30 Core”), and 12 sources with similar properties and available X-Shooter observations with comparable SNR are obtained from the literature (in this paper also referred to as “XQR30 Extended”). This is the first sample with such a high SNR ($\gtrsim 11 - 114$ per bin of 10 km s^{-1} ; D'Odorico et al. 2023) optical/NIR spectra, which allows us for accurate modeling of their emission lines. Out of the total sample, black hole masses and accretion rates for 19 objects are reported for the first time. This work is organized as follows: in Section 2, we describe the sample and we briefly report the data reduction, while in Section 3 we report the spectral modeling; in Section 4 we present our measurements, we compare the black hole masses obtained via C IV and Mg II emission line modeling; we place our work in the context of quasars at lower redshift and we compare them with current measurements of high- z quasars properties in the literature. We list our conclusions and outlook for future studies in Section 5. Throughout the paper, magnitudes are reported in the AB system, and we use a flat cosmology with $H_0 = 70 \text{ km s}^{-1} \text{ Mpc}^{-1}$, $\Omega_M = 0.3$, and $\Omega_\Lambda = 0.7$.

2. Sample and Data Reduction

XQR-30 is an ESO Large Program (Program ID: 1103.A-0817(A); PI: D'Odorico) comprising high SNR ($\sim 11-41$ in

the continuum at rest-frame wavelength of 1285 Å) spectra for 30 high- z quasars with the X-Shooter spectrograph (Ver-net et al. 2011) at the VLT (D'Odorico et al. 2023). The quasars were selected to be observable from Paranal Observatory (Decl. $< 27^\circ$), with redshift in the range $5.8 \lesssim z \lesssim 6.6$, and AB magnitude $J \lesssim 19.8$ (20.0) for $z < 6.0$ ($6.0 \lesssim z \lesssim 6.6$). This survey aims at addressing several goals, from the characterization of the reionization process, to the study of absorbers along the line of sight and the early metal enrichment of the quasars' BLRs and circumgalactic medium (CGM). We also consider 12 additional quasars with analogous luminosities and redshifts, and with X-Shooter spectra with comparable SNR ($\sim 17-114$ at rest-frame 1285 Å) available in the archive (data previously published in Becker et al. 2015, Bosman et al. 2018, Schindler et al. 2020). The spectra for the entire sample were treated with a consistent methodology.

Briefly, the data were reduced with a custom-made pipeline optimized for faint sources (López et al. 2016, Becker et al. 2019). After standard reduction, the correction for telluric absorption is obtained using models created with ESO SKYCALC Cerro Paranal Advanced Sky Model (Noll et al. 2012, Jones et al. 2013). The relative flux calibration is measured with a static response function calculated from a standard star. The 1D stacked spectra of the VIS and NIR arms were combined using Astrocook (Cupani et al. 2018, 2020), and re-binned to a constant velocity step of 50 km s^{-1} . Each quasar's spectrum was absolute-flux calibrated by scaling it to match the observed AB band magnitude in J band (D'Odorico et al. 2023). For a full description of the sample and data reduction, see D'Odorico et al. (2023).

3. Modeling of the spectra

Quasars' rest-frame UV/optical spectra are characterized by a pseudo-continuum, due to different emission processes, and broad emission lines. To model these spectra, we followed the approach described in Mazzucchelli et al. (2017) and Schindler et al. (2020). Details of the spectral modeling will be presented in a forthcoming paper (Bischetti et al. 2023, in prep.), while we summarize in the following the main spectral components:

- a *power-law quasar continuum* emission. For the reddest quasars, we also included a second or third polynomial function to better fit the part of the spectrum blueward of the C IV (e.g. Shen et al. 2019). To model this pseudo continuum, we consider regions of the spectra free of strong emission line features or of absorption due to the atmosphere (e.g. Schindler et al. 2020).
- A *Balmer pseudo continuum* (f_{BC}), as per the description from Dietrich et al. (2003):

$$f_{BC}(\lambda) = f_{BC,0} B_\lambda(\lambda, T_e) \left(1 - e^{\tau_{BE}(\lambda/\lambda_{BE})^3}\right) \quad (1)$$

with values for the electron temperature ($T_e = 15,000 \text{ K}$) and optical depth ($\tau_{BE} = 1$) as used in other works (e.g. De Rosa et al. 2014, Mazzucchelli et al. 2017). We impose the Balmer emission to 30% of the pseudo-continuum contribution, as above described, at rest-frame 3646 Å (e.g. Schindler et al. 2020, Farina et al. 2022). The Balmer pseudo-continuum and the power-law function are modelled at the same time.

- A *Fe II pseudo-continuum*, using the empirical template from Vestergaard & Wilkes (2001), which is used to derive the Mg II emission line-based scaling relation to calculate black hole masses in Section 4. The empirical template, shifted using an initial redshift measured from the Mg II emission line,

is convolved with a Gaussian convolution kernel of different values depending on each spectrum.

- One (or more) Gaussian function(s) is used to model the broad emission lines, with a upper limit to the full-width-at-half-maximum (FWHM) $< 10000 \text{ km s}^{-1}$, which prevents the model from using a very broad Gaussian function to model weak Fe II emission not perfectly reproduced by the Vestergaard & Wilkes (2001) template.

Here, in case the emission lines were fit with more than one Gaussian function, we calculate the best values and uncertainties for the properties of the entire line following the method reported in Schindler et al. (2020). Briefly, for each line for which two or three Gaussian functions were used, we create $N=1000$ replication of each of the best Gaussian fits. For each replication, the mean and standard deviation of each fit are randomly drawn from Gaussian distributions, whose respective mean and standard deviation are fixed to the best fit value and associated uncertainty, respectively. Then, in each replication, we sum the single Gaussian functions and we calculate the total full-width-at-half-maximum (FWHM) as the distance between the two wavelengths where the flux is equal to half the maximum. All the 1000 FWHM values so obtained are distributed as a Gaussian function, and we consider as the best value and uncertainty for the final FWHM of the line the mean and sigma of such distribution. The final $\text{FWHM}_{\text{Mg II}}$ and $\text{FWHM}_{\text{C IV}}$ values are reported in Tab. 1. We show in Fig. 1 the fit of the spectral region around the Mg II emission line. We note that in few cases, the Mg II emission line falls very closely (PSOJ007+04, PSOJ009-10, PSOJ183-12, PSOJ065+01) or within (PSOJ023-02, PSOJ025-11, PSOJ242-12) a region affected by strong telluric absorption. Therefore, also given the potential degeneracies of our spectral modeling with several components, the fit results and relative derived quantities (e.g. black hole masses, bolometric luminosities, Eddington ratios) should be taken with caution.

4. Data Analysis

In this section, we derive the quasars' black hole masses, luminosities and accretion rates, relying on the fit of both the C IV and Mg II wavelength regions.

4.1. Black hole masses and Eddington ratios calculation

Mg II: To derive black hole masses, we use the scaling relation provided by Vestergaard & Osmer (2009):

$$M_{\text{BH,MgII}} = 10^{6.86} \left[\frac{\text{FWHM}_{\text{Mg II}}}{10^3 \text{ km s}^{-1}} \right]^2 \left[\frac{\lambda L_{\lambda}(3000 \text{ \AA})}{10^{44} \text{ erg s}^{-1}} \right]^{0.5} M_{\odot} \quad (2)$$

where $\lambda L_{\lambda}(3000 \text{ \AA})$ is the monochromatic luminosity at rest-frame wavelength 3000 Å. Systematic uncertainties in SMBH masses are estimated to be $\sim 0.55 \text{ dex}$.

C IV: In this case, we use the scaling relation from Vestergaard & Peterson (2006):

$$M_{\text{BH,CIV}} = 10^{6.66} \left[\frac{\text{FWHM}_{\text{C IV,corr}}}{10^3 \text{ km s}^{-1}} \right]^2 \left[\frac{\lambda L_{\lambda}(1350 \text{ \AA})}{10^{44} \text{ erg s}^{-1}} \right]^{0.53} M_{\odot} \quad (3)$$

where the $\lambda L_{\lambda}(1350 \text{ \AA})$ is the monochromatic luminosity at rest-frame wavelength 1350 Å and $\text{FWHM}_{\text{C IV,corr}}$ is the corrected FWHM of the total C IV emission line. It is important to note

that the C IV emission line profile is affected by the presence of an outflowing component (e.g. Richards et al. 2006, Meyer et al. 2019). Therefore, we use the equation from Coatman et al. (2017) to obtain the corrected value of the full-width half maximum:

$$\text{FWHM}_{\text{C IV,corr}} = \frac{\text{FWHM}_{\text{C IV}}}{0.36 \times \frac{\text{C IV Blueshift}}{10^3 \text{ km s}^{-1}} + 0.61} \quad (4)$$

where C IV Blueshift is the velocity difference between the C IV centroid and the quasars' systemic redshifts (obtained from the Mg II or from the [C II] emission line, when available, as reported in D'Odorico et al. 2023, and in Tab. 1), in units of km s^{-1} . In this case, the uncertainties measured on the Vestergaard & Peterson (2006) relation is $\sim 0.40 \text{ dex}$, while it is estimated to be reduced to $\sim 0.24 \text{ dex}$ with the correction by Coatman et al. (2017). We calculated both $L_{\lambda}(1350 \text{ \AA})$ and $L_{\lambda}(3000 \text{ \AA})$ using the value of the fluxes at 1350 Å and 3000 Å from the power-law fit.

From the black hole mass measurements, we can calculate the Eddington luminosity as:

$$L_{\text{Edd,C IV/Mg II}} = 1.3 \times 10^{38} \left(\frac{M_{\text{BH,C IV/Mg II}}}{M_{\odot}} \right) \text{ erg s}^{-1} \quad (5)$$

We also compute the bolometric luminosity (L_{bol}) using the bolometric correction presented by Richards et al. (2006):

$$L_{\text{bol}} = 5.15 \lambda L_{\lambda}(3000 \text{ \AA}) \text{ erg s}^{-1} \quad (6)$$

We note that it has been discussed that such bolometric correction might be overestimated for highly luminous quasars (e.g. Trakhtenbrot & Netzer 2012). Nevertheless, we decide to use it for consistency with several works in the literature (e.g. Mazzucchelli et al. 2017, Yang et al. 2021, Farina et al. 2022). From the L_{Edd} and L_{bol} values we can derive the corresponding Eddington ratios $\lambda_{\text{Edd,C IV}} = L_{\text{bol}}/L_{\text{Edd,C IV}}$ and $\lambda_{\text{Edd,Mg II}} = L_{\text{bol}}/L_{\text{Edd,Mg II}}$. We report the values of the monochromatic and bolometric luminosities, black hole masses and Eddington ratios in Tab. 1.

4.2. C IV vs Mg II black hole masses comparison

We compare the black hole masses measured from the C IV and Mg II emission line regions modeling in Fig. 2. The two measurements are approximately in the same range, although the C IV based values are slightly higher than the Mg II ones, with a mean ratio of $M_{\text{BH,C IV}}/M_{\text{BH,Mg II}} \sim 1.3$. On the other hand, as discussed in Farina et al. (2022), we also notice that the C IV modeling tends to underestimate the values of black hole masses for higher $M_{\text{BH,Mg II}}$ values, i.e. for higher $\text{FWHM}_{\text{Mg II}}$ values. Finally, we also notice that a high fraction of broad absorption line (BAL) quasars have been recovered in the XQR-30 sample ($\sim 50\%$; Bischetti et al. 2022). Even though BAL features may complicate the fit of the C IV emission line region, the high SNR of our spectra still permits a good modeling of the line in the majority of the cases. The quasar PSO J065+01 stands out as a particular outlier, with a C IV-based mass lower than that recovered from the Mg II line by a factor of $\sim 1.3 \text{ dex}$. This is due to the very peculiar shape of the quasar spectrum, and the very low SNR of the C IV emission line.

If one considers the Mg II line-derived BH masses as the reference values, we can estimate the mean (median) of the dispersion of the C IV line-derived values to be **0.28 (0.21) dex**. If one excludes PSOJ065+01, one obtains a mean (median) dispersion

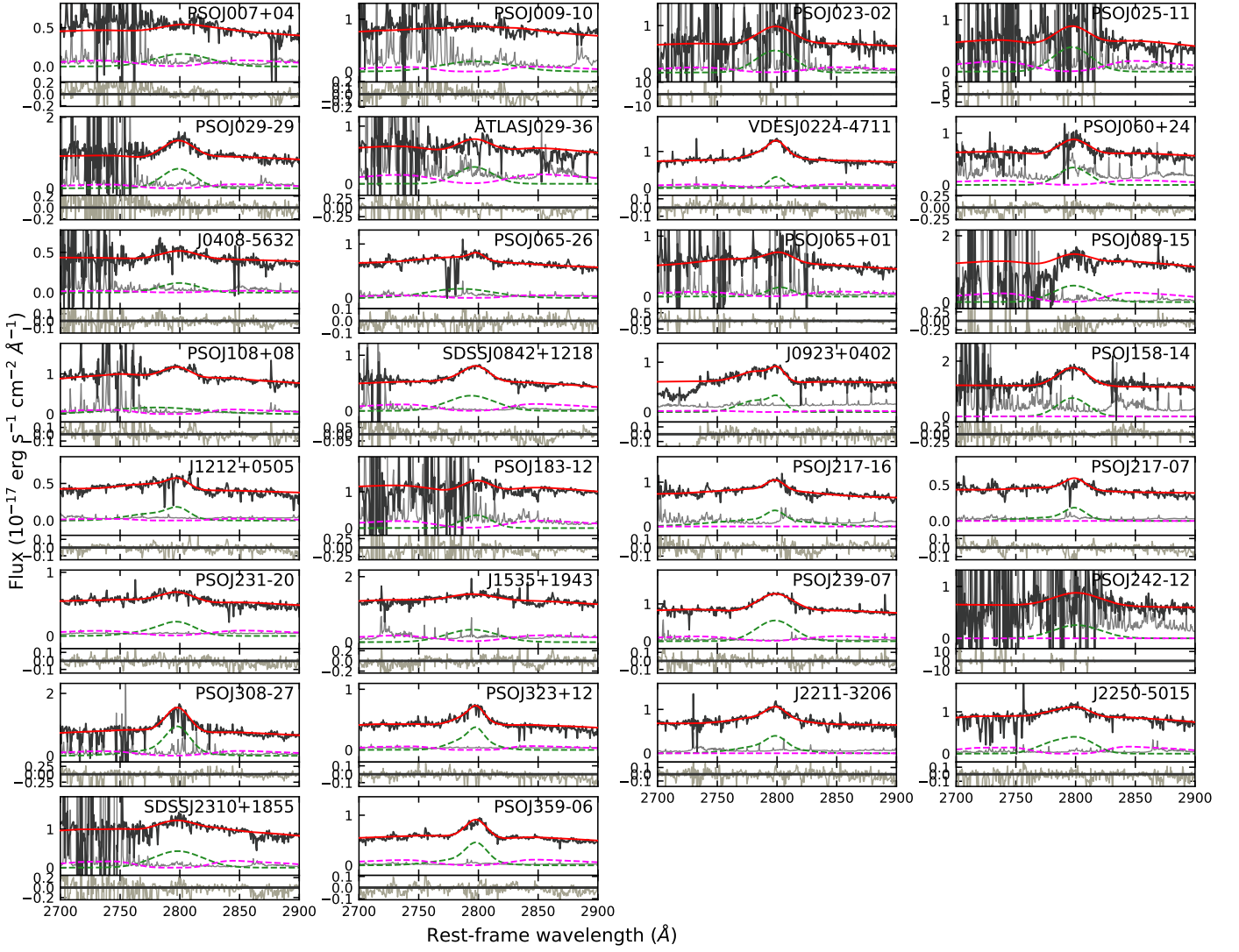


Fig. 1. Spectral region centered on the Mg II emission line for the XQR-30 sample. The pseudo-continuum (power law + Balmer contribution + Fe II empirical template) and multiple Gaussian lines fit are shown with dashed magenta and green lines, respectively, while the total fit is shown in red. We also show the residuals (in grey) in the lower panels. We note that in few cases the Mg II emission line falls partially (PSOJ007+04, PSOJ009-10, PSOJ183-12, PSOJ065+01) or fully (PSOJ023-02, PSOJ025-11, PSOJ242-12) in a region affected by telluric absorption. Despite the general high SNR of our spectra, given the (much) higher noise in these regions, the fit of these objects could be affected.

of 0.25 (0.21) dex. All these values are lower than the dispersion of the C IV-based scaling relation to obtain black hole masses (see Eq. 3), expected to be ~ 0.40 dex from the Vestergaard & Peterson (2006) relation, and are consistent with the ~ 0.24 dex scattering expected when considering the Coatman et al. (2017) correction. A larger black hole masses range would be needed to fully understand how the C IV- and Mg II-based black hole masses estimates compare.

4.3. Comparison with the literature and lower redshift samples

We place our black hole mass and Eddington ratio measurements, based on the Mg II modeling, in the context of the literature (e.g. Yang et al. 2021, Farina et al. 2022). For simplicity, in the following section, we will denominate these quantities as M_{BH} and λ_{BH} .

To consider sources at low redshift, we take the SDSS Data Release 7 (DR7, Richards et al. 2011) quasar catalog. We se-

lect objects with: *a*) redshift between $0.35 < z < 2.25$, i.e. with the Mg II emission line region recovered in the SDSS wavelength range; *b*) valid values for $L_{\lambda}(3000)$; *c*) broad Mg II emission line ($\text{FWHM}_{\text{Mg II}} > 1000 \text{ km s}^{-1}$), with spectra of good quality and hence reliable fit ($\text{FWHM}_{\text{Mg II}} > 2 \text{ ERR_FWHM}_{\text{Mg II}}$ and $\text{EW}_{\text{Mg II}} > 2 \text{ ERR_EW}_{\text{Mg II}}$). The sample so-obtained is of 77,824 quasars. Regarding the high-redshift sample, we consider quasars at $z > 5.8$ with NIR spectra observed in the literature (Willott et al. 2010, De Rosa et al. 2011, Mazzucchelli et al. 2017, Chehade et al. 2018, Shen et al. 2019, Matsuoka et al. 2019, Reed et al. 2019, Onoue et al. 2019, Andika et al. 2020, Eilers et al. 2020, Schindler et al. 2020, Bañados et al. 2021, Yang et al. 2021, Farina et al. 2022; see Fan et al. 2022 for a review). We obtained 114 sources, out of which 23 are also part of the E-XQR-30 sample. We report in Section 4.4 a comparison between the values obtained in this work and in the literature, showing an overall agreement. For the remaining part of the analysis presented below, we consider for these quasars the values of M_{BH} , L_{bol} and λ_{BH} newly derived here. In the fol-

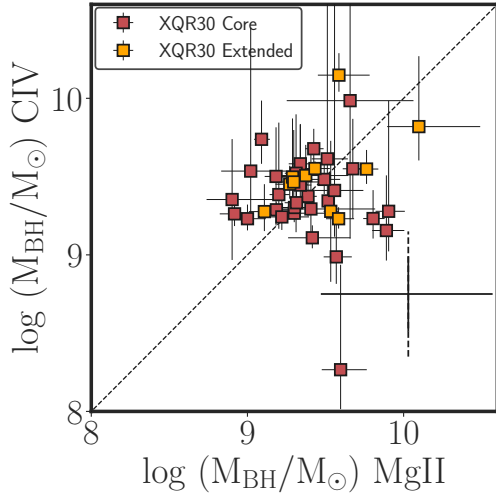


Fig. 2. Comparison between CIV- and Mg II-based black hole masses. Typical uncertainties due to the scatter in the relations used are shown with a black cross in the right-bottom corner. Uncertainties on the uncorrected Vestergaard & Peterson (2006) scaling relations (~ 0.40 dex) are shown with dashed lines.

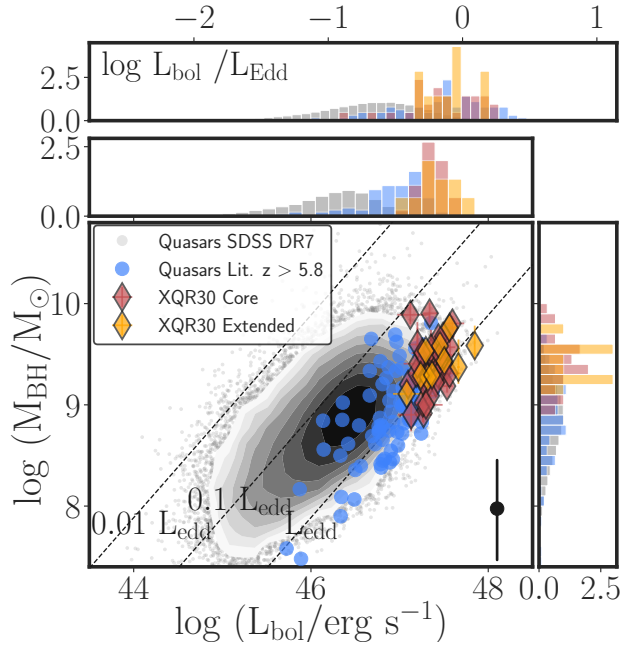


Fig. 3. Black hole masses versus bolometric luminosities. We show quasars at $0.35 < z < 2.25$ from the SDSS DR7 survey (black contours and grey points), and a sample of $z > 5.8$ quasars from the literature (blue points, see Section 4.3 for references). We report the newly calculated values for the core XQR-30 quasars in red diamonds, and the additional 12 high- z sources in golden diamonds. Typical systematic uncertainty on black hole masses, due to the scaling relations used (~ 0.55 dex), is shown in the bottom right corner. Distributions of bolometric luminosities, black hole masses and Eddington ratios for all the above described samples are also reported.

lowing comparison, we exclude the quasar J0100+2802, which is a strong outlier in bolometric luminosity and does not have comparable counterparts in the SDSS survey, and the quasar J0439+1634, which is gravitationally lensed (Fan et al. 2019). Hence, the total sample of high redshift quasars considered here

(literature + E-XQR-30) is of 133 sources. For both the high- z quasars from the literature and the low-redshift objects from SDSS, we calculate the values of black hole masses, bolometric luminosities and Eddington ratios in a consistent way with the sample presented in this paper (see Sec. 4.1). We show in Fig. 3 the black hole masses and bolometric luminosities values for the E-XQR-30 sample and for these comparison samples. As already expected from the sample selection, we see that the E-XQR-30 sample occupies the parameter space at the highest luminosities, with a mean (median) L_{bol} value of 2.3 (2.2) $\times 10^{47}$ erg s $^{-1}$. The mean (median) M_{BH} values are of 2.9 (2.4) $\times 10^9 M_{\odot}$, and mean (median) λ_{BH} values of 0.84 (0.72).

In general, caution should be taken when comparing different quasars sample. First of all, it is extremely difficult to define the completeness of the high- z sample, due to the heterogeneous selection criteria of the different sub-samples (e.g. Bañados et al. 2016, Jiang et al. 2016, Matsuoka et al. 2019). This can insert systematic biases in our comparison, considering that even well defined samples can be biased (for instance a positive luminosity-dependent bias of measured black hole masses has been found; e.g. Shen & Kelly 2012, Kelly & Shen 2013, Wu et al. 2022). Secondly, we would like to highlight that, given that we derived L_{bol} using the bolometric correction from Richards et al. (2006), these values are a reflection of the quasars UV luminosities. Hence, when we match samples by bolometric luminosity distribution (see below), we are effectively considering the intrinsic UV luminosity distribution. Finally, our cut of $\text{FWHM}_{\text{MgII}} > 1000$ km s $^{-1}$ in the low-redshift quasars selection, despite being generally considered in literature for defining broad emission lines objects (e.g. Padovani 2017), can insert a bias against slightly lower FWHM values, which in return affects BHs with lower masses. Keeping in mind these cautions, we still decide to compare the high-redshift quasars sample and the quasars at lower redshifts, in order to test for any redshift evolution in the black hole and Eddington ratio distributions.

We first consider only the sources in the E-XQR30 sample, then we utilize all high- z quasars (from this work + the literature). In order to obtain a consistent comparison, we select a subsample of quasars from the SDSS matching the bolometric luminosity distribution of the sample of quasars at high- z . In practice, we select sources at low- z in a range of $\pm 0.01 \log L_{\text{bol}}$ for each high- z quasar, and we consider their respective M_{BH} and λ_{BH} : we repeat this trial 1000 times. The mean (median) of the black hole masses values of the low- z quasar sample matched with the E-XQR30 sources are 3.2 (2.6) $\times 10^9 M_{\odot}$. On the other hand, the mean (median) λ_{BH} values are 0.86 (0.69). We note that these values are comparable with those obtained for the E-XQR30 objects. We also performed a Kolmogorov-Smirnov (KS) test in order to assess if the bolometric-luminosity matched low- z and the E-XQR30 samples are consistent to be drawn from the same underlying population. We obtain a p value of $0.41 / 0.27$ for the $M_{\text{BH}} / \lambda_{\text{BH}}$ distribution, rejecting the hypothesis that these two samples are not drawn from the same population.

We now consider the entire high- z sample (this work + literature; 133 objects). In order to test how our comparison relies on the intrinsic high-redshift quasars luminosity distribution, we repeat the same comparison as above in different ranges of luminosity, following the approach from Farina et al. (2022). We consider three luminosity ranges each containing the same number of quasars: high luminosity ($\log L_{\text{bol}} > 47.17$ erg s $^{-1}$), medium luminosity ($46.92 < \log L_{\text{bol}} < 47.17$ erg s $^{-1}$) and low luminosity ($\log L_{\text{bol}} < 46.92$ erg s $^{-1}$). Results are reported in Fig. 4. The mean, median, and standard deviation values for L_{bol} , M_{BH}

and λ_{BH} , for the entire luminosity sample, and for each range of luminosity, for the low- and high- z samples are listed in Tab. 2. We repeated the KS test for this sample, and for all the luminosity ranges. The resulting p-values are also reported in Tab. 2.

We note that the bolometric luminosity distribution in the low- z sample is constructed to be consistent with that at high- z . This is also reflected in the corresponding p-values of 1 for all the cases (see Tab. 2). We find that the mean and median black hole mass/Eddington ratio values are lower/higher in the high-redshift sample with respect to the low- z one, considering all luminosities, and in every luminosity range. However, we note that these differences with redshifts are more significant at lower luminosities, with a difference between the mean Eddington ratio at high- and low- z of ~ 0.38 in the low luminosity range, higher with respect to what is observed for luminous objects (~ 0.03). We can also notice that the distributions of M_{BH} and λ_{BH} have slightly larger dispersions at lower luminosities. E.g. the standard deviation for the high- z black hole masses (Eddington ratios) is 0.45 (0.38) dex in the low luminosity range, with respect to a standard deviation of 0.25 (0.24) dex in the high luminosity range. These trends can also be reflected in the results of the KS test. Indeed, in the high luminosity range, the p-values obtained by comparing the black hole masses and Eddington ratios distributions at high- and low- z are relatively high (0.47 and 0.32, respectively). Conversely, in the medium and low luminosity ranges, and when considering all luminosities, we recover low p-values ($< 10^{-4}$), rejecting the hypothesis that these quantities are drawn from the same underlying distribution.

In summary, our analysis suggests that quasars at high redshift accrete slightly faster than those in a bolometric luminosity distribution matched sample at $z \sim 1.5$, assuming the same mean radiative efficiency. This trend increases for the faintest objects discovered, albeit with a larger dispersion. In other words, at high-redshift we observe that the most luminous quasars are powered by less massive SMBHs, accreting at slightly higher rates compared to a luminosity-matched sample at high- z . This result is in contrast with respect to previous works (e.g. Mazzucchelli et al. 2017, Shen et al. 2019), which did not recover a change in the mean Eddington ratio value with z , and with expectations from the consistency between composite spectra of quasars at $z \gtrsim 6$ and at lower- z (e.g. Shen et al. 2019, Yang et al. 2021). On the other hand, our outcome is in agreement with the recent results by Yang et al. (2021) and Farina et al. (2022), which observed a similar increase in the mean value of the Eddington ratio as measured in this work. Also, one can notice that the composite spectra obtained in the literature are usually focused on the higher luminosity quasars, both at high- and low- z (e.g. Vanden Berk et al. 2001, Selsing et al. 2016), where the changes between the two samples are less apparent (see Fig. 4 and Tab. 2).

4.4. Comparison between XQR-30 and literature values

We note that 23 objects reported in the E-XQR-30 sample already have observations reported in the literature. In case of sources observed by more than one study, we consider only the most recent measurement: J0142-3327 (Chehade et al. 2018); PSO060+24 (Shen et al. 2019); J0224-4711 (Reed et al. 2019); J0923+0402, J1535+1943 (Yang et al. 2021); PSO239-07, J2211-3206, J0842+1218, PSO231-20, PSO158-14, PSO007+04, PSO065-26, PSO183+05, J2310+1855, PSOJ359-06, PSOJ323+12, J1319+0950, PSO036+03, J1030+0524, J1306+0356, J1509-1749, J0100+2802 (Farina et al. 2022). The quasar J0439+1634 was also observed by Yang et al. (2021), but

given that this source is lensed (Fan et al. 2019), we decide to not include it in this comparison. We show in Fig. 5 the comparison of the bolometric luminosities, black hole masses and Eddington ratios (from the Mg II emission line model), all calculated with a consistent method (see Section 4.1). In general, we note that there are no recovered systemic trends between the quantities derived here and those from the literature. The major outlier reported here is PSOJ007+04, whose Mg II emission line was fitted in this work with a very broad Gaussian (see Tab. 1 and Fig. 1). This resulted in a very large black hole mass and a low Eddington ratio, differently than what presented in Farina et al. (2022). This is due to the fact that the Mg II line in this quasar is very close to a telluric absorption, hence its modelling should be considered with caution (see Fig. 1 and Tab. 1).

5. Conclusions

The E-XQR-30 sample provides us with a unique opportunity to study quasars at high- z with spectra of exquisite quality and high signal-to-noise ratio. Here, we calculate their bolometric luminosities via the monochromatic luminosity at rest frame 3000 Å. We obtain black hole mass values by modeling the C IV and Mg II emission line regions, using scaling relation calibrated in the local universe (Vestergaard & Peterson 2006, Vestergaard & Osmer 2009). In particular, we account for the non-virial component of the C IV emission line, due to outflows/wings, utilizing the correction from Coatman et al. (2017). We observe that, in our sample, the black hole mass values obtained with the two emission lines cover the same parameter space (see Fig. 2). Assuming that the Mg II-based estimates are the more reliable, the scatter of the C IV-based measurements is lower than that measured around the Vestergaard & Peterson (2006) scaling relation (~ 0.4 dex), and it is consistent/slightly larger than what is expected after the Coatman et al. (2017) correction (~ 0.24 dex).

We compare the values measured from the E-XQR-30 objects with those of other quasars at $z > 5.8$ obtained from the literature, and from a sample of quasars at $0.35 < z < 2.25$ from the SDSS DR7 survey (see Fig. 3). We consider a comparison sub-sample of quasars at low- z , matched to the entire high- z quasars' bolometric luminosity distribution. The high-redshift Eddington ratio distribution is slightly higher with respect to the matched low- z sample (i.e. with a difference between the mean λ_{BH} values of ~ 0.27 ; see Fig. 4 and Tab. 2). We repeat this comparison considering sub-samples of high- and low- z quasars in different bolometric luminosity ranges, and noted that this increase in the mean Eddington ratio at higher redshifts is present in every luminosity range, and is more marked at lower luminosities. This suggests that quasars at $z \gtrsim 6$ accrete marginally faster than at $z \sim 1$, as suggested by other recent works in the literature (e.g. Yang et al. 2021, Farina et al. 2022).

In the future, it will be crucial to explore the properties of quasars over larger ranges of luminosity and black hole masses, thanks also to the discoveries that will be enabled by future surveys such as the Legacy Survey of Space and Time (LSST) at Vera Rubin Observatory (e.g. Ivezić et al. 2014, 2019) and the Euclid survey (e.g. Euclid Collaboration et al. 2019). On the other hand, it will also be important to measure black hole masses from other emission lines, e.g. H β , which are directly related to the reverberation mapping studies at low- z , and test whether there are any systematic difference with values obtained from the C IV or Mg II line modeling (e.g. Homayouni et al. 2020). The James Webb Telescope will be key in pursuing such studies (e.g. Eilers et al. 2023, Larson et al. 2023, Yang et al. 2023, Maiolino et al. 2023).

Table 1. Enlarged XQR-30 Sample: Redshift derived from the Mg II emission line modeling or, when available, from the [C II] emission line (see D’Odorico et al. 2023); C IV and Mg II full-width at half maximum; C IV blueshift (used in equation 4); monochromatic luminosities at rest-frame 1350 Å and 3000 Å; bolometric luminosities; black hole masses and Eddington ratio values, derived from both the C IV and Mg II emission lines.

Name	Redshift	FWHM _{CIV} [km s ⁻¹]	FWHM _{MgII} [km s ⁻¹]	C IV Blueshift [km s ⁻¹]	log \mathcal{L}_{1350} [erg s ⁻¹]	log \mathcal{L}_{3000} [erg s ⁻¹]	log L_{bol} [erg s ⁻¹]	log $M_{\text{BH,C IV}}$ [M_{\odot}]	log $M_{\text{BH, Mg II}}$ [M_{\odot}]	$\lambda_{\text{Edd,C IV}}$	$\lambda_{\text{Edd,Mg II}}$
PSOJ007+04 ^{a)}	6.0015 [†]	6169±1057	8176±473	2778±601	46.56 ^{+0.05} _{-0.06}	46.41 ^{+0.15} _{-0.22}	47.12 ^{+0.15} _{-0.22}	9.16 ^{+0.19} _{-0.22}	9.89 ^{+0.09} _{-0.11}	0.71±0.49	0.13±0.06
PSOJ009-10 ^(a)	6.004 [†]	802±2963	7336±697	2956±456	46.42 ^{+0.06} _{-0.08}	46.63 ^{+0.02} _{-0.09}	47.34 ^{+0.08} _{-0.09}	9.28 ^{+0.26} _{-0.11}	9.9 ^{+0.08} _{-0.05}	0.88±0.73	0.21±0.06
PSOJ023-02 ^(a)	5.90	4806±486	4065±201	832±112	46.39 ^{+0.05} _{-0.06}	46.62 ^{+0.02} _{-0.09}	47.33 ^{+0.06} _{-0.09}	9.37 ^{+0.18} _{-0.11}	9.39 ^{+0.05} _{-0.05}	0.7±0.26	0.68±0.12
PSOJ025-11 ^{a)}	5.85	5283±1043	3976±196	1316±286	46.68 ^{+0.03} _{-0.04}	46.56 ^{+0.03} _{-0.04}	47.27 ^{+0.03} _{-0.04}	9.45 ^{+0.39} _{-0.18}	9.34 ^{+0.06} _{-0.06}	0.51±0.32	0.66±0.18
PSOJ029-29	5.984	6886±1190	3501±292	2063±285	46.88 ^{+0.02} _{-0.03}	46.78 ^{+0.03} _{-0.08}	47.49 ^{+0.01} _{-0.08}	9.58 ^{+0.16} _{-0.25}	9.34 ^{+0.07} _{-0.09}	0.63±0.3	1.1±0.27
ATLASJ029-36	6.02	5808±1517	3753±266	1924±377	46.73 ^{+0.01} _{-0.01}	46.38 ^{+0.03} _{-0.03}	47.1 ^{+0.03} _{-0.06}	9.39 ^{+0.22} _{-0.16}	9.2 ^{+0.06} _{-0.06}	0.4±0.26	0.6±0.1
VDESJ0224-4711	6.526	5378±207	2863±206	1808±42	46.61 ^{+0.03} _{-0.04}	46.82 ^{+0.03} _{-0.08}	47.54 ^{+0.06} _{-0.06}	9.29 ^{+0.25} _{-0.16}	9.19 ^{+0.08} _{-0.08}	1.36±0.23	1.72±0.36
PSOJ060+24	6.18	4522±625	3270±249	633±323	46.58 ^{+0.03} _{-0.04}	46.59 ^{+0.08} _{-0.11}	47.3 ^{+0.1} _{-0.1}	9.5 ^{+0.31} _{-0.08}	9.18 ^{+0.07} _{-0.07}	0.48±0.52	1.01±0.27
J0408-5632 [‡]	6.0345	6943±355	4057±323	2411±155	46.55 ^{+0.04} _{-0.04}	46.48 ^{+0.08} _{-0.11}	47.19 ^{+0.08} _{-0.11}	9.33 ^{+0.07} _{-0.08}	9.31 ^{+0.08} _{-0.09}	0.55±0.15	0.57±0.16
PSOJ065-26	6.1871 [†]	8866±2638	4878±836	3895±1503	46.83 ^{+0.01} _{-0.01}	46.64 ^{+0.04} _{-0.08}	47.35 ^{+0.04} _{-0.04}	9.41 ^{+0.3} _{-0.08}	9.56 ^{+0.13} _{-0.13}	0.67±0.66	0.48±0.17
PSOJ065+01 ^(ab)	5.79	2389±878	5569±849	2682±368	46.4 ^{+0.03} _{-0.03}	46.49 ^{+0.03} _{-0.06}	47.2 ^{+0.1} _{-0.1}	8.27 ^{+0.25} _{-0.16}	9.6 ^{+0.15} _{-0.17}	6.63±5.37	0.31±0.12
PSOJ089-15 [‡]	5.957	3345±707	4365±425	1385±164	46.6 ^{+0.05} _{-0.04}	46.86 ^{+0.05} _{-0.06}	47.57 ^{+0.05} _{-0.06}	8.99 ^{+0.17} _{-0.22}	9.57 ^{+0.08} _{-0.08}	2.94±1.48	0.77±0.18
PSOJ108+08	5.9485	8164±628	4247±346	3109±281	46.84 ^{+0.04} _{-0.04}	46.75 ^{+0.1} _{-0.03}	47.46 ^{+0.1} _{-0.03}	9.48 ^{+0.09} _{-0.09}	9.49 ^{+0.08} _{-0.08}	0.74±0.26	0.72±0.24
SDSSJ0842+1218 [‡]	6.0754 [†]	6041±270	3854±337	2078±37	46.58 ^{+0.02} _{-0.02}	46.54 ^{+0.03} _{-0.03}	47.25 ^{+0.03} _{-0.03}	9.3 ^{+0.09} _{-0.07}	9.42 ^{+0.06} _{-0.06}	0.68±0.11	0.68±0.15
J0923+0402 [‡]	6.633 [†]	5940±327	3793±799	2682±135	46.5 ^{+0.07} _{-0.08}	46.79 ^{+0.08} _{-0.11}	47.51 ^{+0.08} _{-0.13}	9.11 ^{+0.38} _{-0.31}	9.31 ^{+0.24} _{-0.24}	1.92±0.45	0.95±0.44
PSOJ158-14	6.0685 [†]	6323±1538	3258±212	1767±138	46.77 ^{+0.06} _{-0.08}	46.85 ^{+0.1} _{-0.13}	47.56 ^{+0.13} _{-0.13}	9.52 ^{+0.38} _{-0.38}	9.41 ^{+0.21} _{-0.21}	0.85±1.19	1.37±0.42
PSOJ183+05	6.4386 [†]	7075±2010	4476±1282	3035±348	46.69 ^{+0.08} _{-0.08}	46.49 ^{+0.16} _{-0.16}	47.2 ^{+0.16} _{-0.16}	9.29 ^{+0.21} _{-0.21}	9.41 ^{+0.08} _{-0.08}	0.62±0.47	0.48±0.36
PSOJ183-12 ^(a)	5.86	6196±517	3203±517	3031±194	46.81 ^{+0.05} _{-0.05}	46.7 ^{+0.07} _{-0.07}	47.41 ^{+0.06} _{-0.06}	9.24 ^{+0.12} _{-0.12}	9.22 ^{+0.12} _{-0.12}	1.13±0.29	1.19±0.43
PSOJ217-16	6.1498 [†]	10292±909	2772±741	3243±1394	46.6 ^{+0.04} _{-0.04}	46.55 ^{+0.08} _{-0.08}	47.26 ^{+0.08} _{-0.08}	9.54 ^{+0.27} _{-0.27}	9.02 ^{+0.34} _{-0.34}	0.41±0.37	1.34±0.79
PSOJ217-07 [‡]	6.1663	9174±2402	2607±533	3260±2169	46.46 ^{+0.07} _{-0.07}	46.42 ^{+0.15} _{-0.15}	47.13 ^{+0.15} _{-0.15}	9.35 ^{+0.39} _{-0.39}	8.9 ^{+0.16} _{-0.16}	0.46±0.69	1.3±0.8
PSOJ231-20 [‡]	6.5869 [†]	6470±241	4644±179	2528±116	46.74 ^{+0.01} _{-0.01}	46.65 ^{+0.04} _{-0.04}	47.36 ^{+0.04} _{-0.04}	9.34 ^{+0.05} _{-0.05}	9.52 ^{+0.04} _{-0.04}	0.79±0.12	0.53±0.07
J1535+1943	6.370 [†]	6268±654	5640±236	3353±271	46.51 ^{+0.01} _{-0.01}	46.88 ^{+0.13} _{-0.13}	47.6 ^{+0.13} _{-0.13}	9.23 ^{+0.18} _{-0.18}	9.8 ^{+0.07} _{-0.07}	1.78±0.77	0.48±0.15
PSOJ239-07 [‡]	6.1102 [†]	4863±185	3947±79	537±63	46.72 ^{+0.03} _{-0.03}	46.74 ^{+0.13} _{-0.13}	47.46 ^{+0.13} _{-0.13}	9.68 ^{+0.13} _{-0.13}	9.42 ^{+0.06} _{-0.06}	0.46±0.17	0.83±0.24
PSOJ242-12 ^{a)}	5.830	6791±1672	4892±495	1152±439	46.48 ^{+0.09} _{-0.08}	46.55 ^{+0.13} _{-0.13}	47.26 ^{+0.13} _{-0.13}	9.61 ^{+0.23} _{-0.23}	9.51 ^{+0.1} _{-0.1}	0.34±0.33	0.43±0.18
PSOJ308-27	5.7985	5284±148	2852±131	535±115	46.7 ^{+0.02} _{-0.02}	46.64 ^{+0.06} _{-0.06}	47.35 ^{+0.06} _{-0.06}	9.74 ^{+0.16} _{-0.16}	9.09 ^{+0.08} _{-0.08}	0.32±0.14	1.4±0.26
PSOJ323+12	6.5872 [†]	2828±140	2450±284	326±27	46.65 ^{+0.02} _{-0.02}	46.56 ^{+0.07} _{-0.07}	47.27 ^{+0.07} _{-0.07}	9.26 ^{+0.08} _{-0.08}	8.92 ^{+0.15} _{-0.15}	0.78±0.19	1.73±0.5
VIK J2211-3206 [‡]	6.3394 [†]	5114±224	3448±729	1811±97	46.66 ^{+0.03} _{-0.03}	46.73 ^{+0.05} _{-0.05}	47.44 ^{+0.05} _{-0.05}	9.27 ^{+0.08} _{-0.08}	9.3 ^{+0.15} _{-0.15}	1.15±0.2	1.06±0.47
VDES J2250-5051 [‡]	5.9767	16618±11883	5212±4022	3001±9685	46.58 ^{+0.04} _{-0.04}	46.73 ^{+0.05} _{-0.05}	47.44 ^{+0.05} _{-0.05}	9.99 ^{+0.88} _{-0.88}	9.66 ^{+0.41} _{-0.41}	0.22±1.45	0.46±0.72
SDSSJ2310+18 [‡]	6.0031 [†]	8576±2362	5156±252	3224±1504	46.92 ^{+0.03} _{-0.03}	46.78 ^{+0.08} _{-0.13}	47.49 ^{+0.13} _{-0.13}	9.55 ^{+0.32} _{-0.32}	9.67 ^{+0.08} _{-0.08}	0.67±0.75	0.51±0.15
PSOJ359-06	6.1722 [†]	3257±142	2653±213	554±39	46.55 ^{+0.08} _{-0.08}	46.59 ^{+0.13} _{-0.13}	47.3 ^{+0.13} _{-0.13}	9.23 ^{+0.09} _{-0.09}	9.0 ^{+0.12} _{-0.12}	0.9±0.36	1.53±0.65
SDSSJ0100+28	6.3268 [†]	6647±1971	5742±1705	2496±316	47.58 ^{+0.01} _{-0.01}	47.44 ^{+0.04} _{-0.04}	48.15 ^{+0.04} _{-0.04}	9.82 ^{+0.22} _{-0.22}	10.1 ^{+0.2} _{-0.2}	2.94±1.48	0.77±0.52
ATLASJ025-33	6.3373 [†]	6408±962	3302±768	2461±251	47.03 ^{+0.01} _{-0.01}	46.95 ^{+0.02} _{-0.02}	47.66 ^{+0.02} _{-0.02}	9.51 ^{+0.13} _{-0.13}	9.37 ^{+0.17} _{-0.17}	0.88±0.73	0.21±0.7
ULASJ0148+06	5.977	5811±368	4741±473	2906±129	46.85 ^{+0.01} _{-0.01}	46.74 ^{+0.04} _{-0.04}	47.46 ^{+0.04} _{-0.04}	9.23 ^{+0.06} _{-0.06}	9.58 ^{+0.08} _{-0.08}	0.7±0.26	0.68±0.13
PSOJ036+03	6.5405 [†]	10131±329	3872±367	3727±135	46.82 ^{+0.01} _{-0.01}	46.79 ^{+0.05} _{-0.05}	47.5 ^{+0.05} _{-0.05}	9.55 ^{+0.03} _{-0.03}	9.43 ^{+0.08} _{-0.08}	0.51±0.32	0.66±0.2
QSOJ0439+1634 ^{c)}	6.5188 [†]	5352±110	3329±295	1773±58	47.51 ^{+0.02} _{-0.02}	47.62 ^{+0.03} _{-0.03}	48.33 ^{+0.03} _{-0.03}	9.77 ^{+0.04} _{-0.04}	9.72 ^{+0.07} _{-0.07}	0.63±0.3	1.1±0.62
SDSSJ0818+17	5.96	9869±805	5477±334	3727±329	46.86 ^{+0.04} _{-0.04}	46.85 ^{+0.08} _{-0.08}	47.56 ^{+0.08} _{-0.08}	9.55 ^{+0.1} _{-0.1}	9.76 ^{+0.09} _{-0.09}	0.4±0.26	0.6±0.13
SDSSJ0836+00	5.773	6908±196	3793±691	573±77	47.06 ^{+0.04} _{-0.04}	47.14 ^{+0.06} _{-0.06}	47.85 ^{+0.06} _{-0.06}	10.15 ^{+0.11} _{-0.11}	9.59 ^{+0.07} _{-0.07}	1.36±0.23	1.72±0.51
SDSSJ0927+20	5.7722 [†]	5480±732	3405±243	1785±166	46.55 ^{+0.03} _{-0.03}	46.37 ^{+0.15} _{-0.15}	47.08 ^{+0.15} _{-0.15}	9.28 ^{+0.14} _{-0.14}	9.11 ^{+0.08} _{-0.08}	0.48±0.52	1.01±0.36
SDSSJ1030+05	6.304	5002±391	3578±336	1092±92	46.64 ^{+0.08} _{-0.08}	46.61 ^{+0.11} _{-0.11}	47.32 ^{+0.11} _{-0.11}	9.45 ^{+0.08} _{-0.08}	9.27 ^{+0.09} _{-0.09}	0.55±0.15	0.57±0.31
SDSSJ1306+03	6.033 [†]	4567±688	3825±449	769±189	46.66 ^{+0.02} _{-0.02}	46.53 ^{+0.05} _{-0.05}	47.24 ^{+0.05} _{-0.05}	9.5 ^{+0.12} _{-0.12}	9.29 ^{+0.09} _{-0.09}	0.67±0.66	0.48±0.19
ULASJ1319+09	6.1347 [†]	6964±2636	4905±162	3150±2607	46.73 ^{+0.03} _{-0.03}	46.58 ^{+0.09} _{-0.09}	47.3 ^{+0.09} _{-0.09}	9.28 ^{+0.15} _{-0.15}	9.53 ^{+0.08} _{-0.08}	0.71±0.49	0.13±0.09
CFHQSJ1509-1	6.1225 [†]	5095±828	3586±707	1021±216	46.59 ^{+0.04} _{-0.04}	46.65 ^{+0.08} _{-0.08}	47.37 ^{+0.08} _{-0.08}	9.47 ^{+0.13} _{-0.13}	9.3 ^{+0.11} _{-0.11}	6.63±5.37	0.31±0.39

Notes. † Redshift from [CII] emission line (see D’Odorico et al. 2023). ‡ Classified as a Broad Absorption Line (BAL) quasar (Bischoff et al. 2022).

a) Note that the Mg II emission line in this spectrum is very close to/within a strong telluric feature, therefore it needs to be taken with caution.

b) Note that the C IV emission line region in this spectrum has low SNR, therefore the derived black holes and Eddington ratios need to be taken with caution.

c) This quasar is gravitationally lensed (Fan et al. 2019); the values presented here are not corrected for magnification. This quasar was not included in the comparison with lower- z sources in the discussion session.

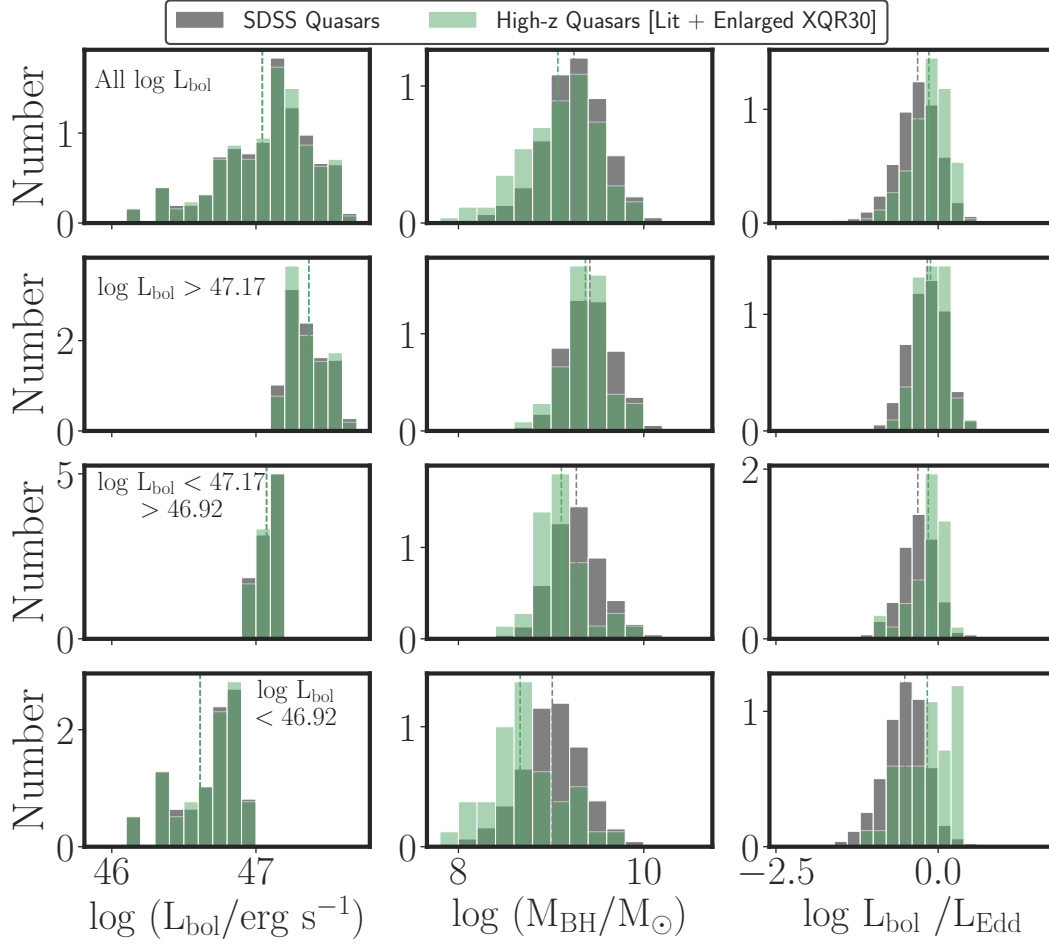


Fig. 4. Bolometric Luminosities (*left*), black hole masses (*middle*) and Eddington ratios (*right*) distributions for all the quasars at high- z (literature + enlarged XQR-30) in green, and for a bolometric luminosity matched sample at low- z . Mean values for the quantities, both at low- and high-redshift, are shown with dashed lines, in grey and green, respectively. In the *top* row we consider all the luminosity distribution of high- z quasars, while from the *second* to the *last* row we present the samples divided by luminosity ranges, each containing the same number of high- z quasars, from high to medium to low luminosities. See Section 4.3 for further details on the samples compilation and matching. The Eddington ratio distribution at high- z is shifted to marginally higher values than at lower- z , for the entire luminosity case, and for each luminosity range. We note that with decreasing luminosity, the separation between the high and low redshift sample is increasing, albeit with larger dispersions.

Table 2. Mean, median and standard deviation of bolometric luminosities, black hole masses and Eddington ratios distribution shown in Figure 4, for the low- and high- z quasars samples. We also report the p-values obtained with a Kolmogorov-Smirnov test.

	High- z quasars			Low- z quasars			KS-test p-value
	mean	median	st.dev	mean	median	st.dev	
All Luminosity							
$L_{\text{bol}} [10^{47} \text{ erg s}^{-1}]$	1.49	1.32	0.38	1.49	1.32	0.38	1
$M_{\text{BH}} [10^9 M_{\odot}]$	1.79	1.40	0.45	2.44	1.80	0.35	2×10^{-4}
λ_{BH}	0.89	0.76	0.30	0.62	0.50	0.34	2×10^{-8}
High luminosity: $L_{\text{bol}} > 10^{47.17} \text{ erg s}^{-1}$							
$L_{\text{bol}} [10^{47} \text{ erg s}^{-1}]$	2.47	2.18	0.14	2.47	2.17	0.14	1.0
$M_{\text{BH}} [10^9 M_{\odot}]$	2.74	2.18	0.25	3.19	2.53	0.28	0.47
λ_{BH}	0.88	0.73	0.24	0.85	0.69	0.28	0.32
Medium luminosity: $10^{46.92} < L_{\text{bol}} < 10^{47.17} \text{ erg s}^{-1}$							
$L_{\text{bol}} [10^{47} \text{ erg s}^{-1}]$	1.20	1.26	0.07	1.20	1.26	0.07	1.0
$M_{\text{BH}} [10^9 M_{\odot}]$	1.61	1.28	0.27	2.38	1.81	0.30	1×10^{-4}
λ_{BH}	0.84	0.76	0.28	0.61	0.51	0.29	6×10^{-5}
Low luminosity: $L_{\text{bol}} < 10^{46.92} \text{ erg s}^{-1}$							
$L_{\text{bol}} [10^{47} \text{ erg s}^{-1}]$	0.49	0.58	0.30	0.49	0.58	0.30	1.0
$M_{\text{BH}} [10^9 M_{\odot}]$	0.52	0.52	0.45	1.46	1.03	0.35	10^{-8}
λ_{BH}	0.79	0.77	0.38	0.41	0.32	0.34	3×10^{-9}

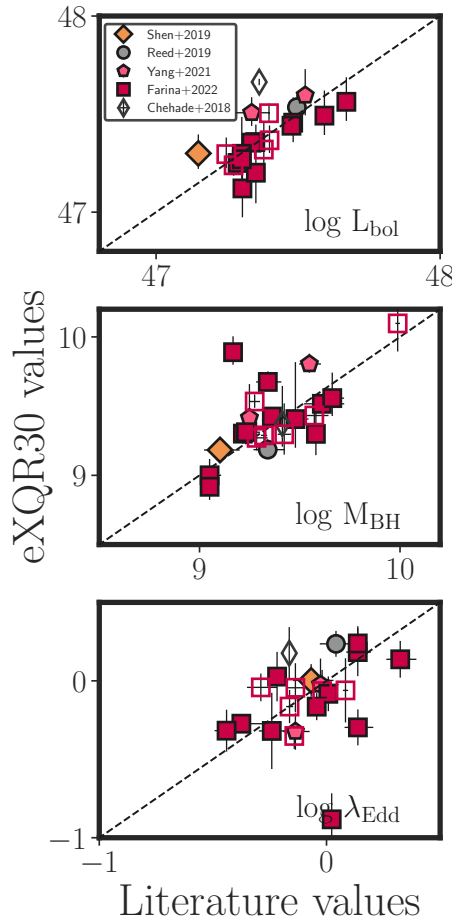


Fig. 5. Comparison between bolometric luminosities (*upper*), black hole masses (*central*) and Eddington ratios (*lower panel*) for the quasars in the enlarged XQR-30 sample that were previously observed and studied in the literature: black diamond (Chehade et al. 2018), yellow diamond (Shen et al. 2019), grey circle (Reed et al. 2019), pink pentagon (Yang et al. 2021) and red squares (Farina et al. 2022). The dashed black line denotes the one-to-one relation. The filled symbols represent data of sources from the core XQR-30 survey, while empty ones show data from the literature sample.

Acknowledgements. G.B. was supported by the National Science Foundation through grant AST-1751404. E.P.F. is supported by the international Gemini Observatory, a program of NSF’s NOIRLab, which is managed by the Association of Universities for Research in Astronomy (AURA) under a cooperative agreement with the National Science Foundation, on behalf of the Gemini partnership of Argentina, Brazil, Canada, Chile, the Republic of Korea, and the United States of America. R.A.M. acknowledge support from the ERC Advanced Grant 740246 (Cosmic_Gas). S.C. is supported by European Union’s HE ERC Starting Grant No. 101040227 - WINGS. This work is based on observations collected at the European Southern Observatory under ESO large program 1103.A-0817(A).

References

Andika, I. T., Jahnke, K., Onoue, M., et al. 2020, *ApJ*, 903, 34
 Bañados, E., Mazzucchelli, C., Momjian, E., et al. 2021, *ApJ*, 909, 80
 Bañados, E., Venemans, B. P., Decarli, R., et al. 2016, *ApJS*, 227, 11
 Bañados, E., Venemans, B. P., Mazzucchelli, C., et al. 2018, *Nature*, 553, 473
 Becker, G. D., Bolton, J. S., Madau, P., et al. 2015, *MNRAS*, 447, 3402
 Becker, G. D., Pettini, M., Rafelski, M., et al. 2019, *ApJ*, 883, 163
 Begelman, M. C., Volonteri, M., & Rees, M. J. 2006, *MNRAS*, 370, 289
 Bischetti, M., Feruglio, C., D’Odorico, V., et al. 2022, *Nature*, 605, 244
 Bond, J. R., Arnett, W. D., & Carr, B. J. 1984, *ApJ*, 280, 825
 Bosman, S. E. I., Fan, X., Jiang, L., et al. 2018, *MNRAS*, 479, 1055
 Chehade, B., Carnall, A. C., Shanks, T., et al. 2018, *MNRAS*, 478, 1649

Coatman, L., Hewett, P. C., Banerji, M., et al. 2017, *MNRAS*, 465, 2120
 Cupani, G., Calderone, G., Cristiani, S., et al. 2018, in *Society of Photo-Optical Instrumentation Engineers (SPIE) Conference Series*, Vol. 10707, Software and Cyberinfrastructure for Astronomy V, ed. J. C. Guzman & J. Ibsen, 1070723
 Cupani, G., D’Odorico, V., Cristiani, S., et al. 2020, in *Society of Photo-Optical Instrumentation Engineers (SPIE) Conference Series*, Vol. 11452, Society of Photo-Optical Instrumentation Engineers (SPIE) Conference Series, 114521U
 Davies, F. B., Hennawi, J. F., & Eilers, A.-C. 2019, *ApJ*, 884, L19
 De Rosa, G., Decarli, R., Walter, F., et al. 2011, *ApJ*, 739, 56
 De Rosa, G., Venemans, B. P., Decarli, R., et al. 2014, *ApJ*, 790, 145
 Denney, K. D., Horne, K., Shen, Y., et al. 2016, *ApJS*, 224, 14
 Devecchi, B. & Volonteri, M. 2009, *ApJ*, 694, 302
 Dietrich, M., Hamann, F., Appenzeller, I., & Vestergaard, M. 2003, *ApJ*, 596, 817
 D’Odorico, V., Bañados, E., Becker, G. D., et al. 2023, *MNRAS*, 523, 1399
 Eilers, A.-C., Hennawi, J. F., Decarli, R., et al. 2020, *ApJ*, 900, 37
 Eilers, A.-C., Simcoe, R. A., Yue, M., et al. 2023, *ApJ*, 950, 68
 Euclid Collaboration, Barnett, R., Warren, S. J., et al. 2019, *A&A*, 631, A85
 Fan, X., Bañados, E., & Simcoe, R. A. 2022, *arXiv e-prints*, arXiv:2212.06907
 Fan, X., Wang, F., Yang, J., et al. 2019, *ApJ*, 870, L11
 Farina, E. P., Schindler, J.-T., Walter, F., et al. 2022, *ApJ*, 941, 106
 Ferrara, A., Salvadori, S., Yue, B., & Schleicher, D. 2014, *MNRAS*, 443, 2410
 Homayouni, Y., Trump, J. R., Grier, C. J., et al. 2020, *ApJ*, 901, 55
 Inayoshi, K., Visbal, E., & Haiman, Z. 2020, *ARA&A*, 58, 27
 Ivezić, Ž., Brandt, W. N., Fan, X., et al. 2014, in *Multiwavelength AGN Surveys and Studies*, ed. A. M. Mickaelian & D. B. Sanders, Vol. 304, 11–17
 Ivezić, Ž., Kahn, S. M., Tyson, J. A., et al. 2019, *ApJ*, 873, 111
 Jiang, L., Fan, X., Ivezić, Ž., et al. 2007, *ApJ*, 656, 680
 Jiang, L., McGreer, I. D., Fan, X., et al. 2015, *AJ*, 149, 188
 Jiang, L., McGreer, I. D., Fan, X., et al. 2016, *ApJ*, 833, 222
 Jones, A., Noll, S., Kausch, W., Szyszka, C., & Kimeswenger, S. 2013, *A&A*, 560, A91
 Kelly, B. C. & Shen, Y. 2013, *ApJ*, 764, 45
 Kurk, J. D., Walter, F., Fan, X., et al. 2007, *ApJ*, 669, 32
 Lai, S., Bian, F., Onken, C. A., et al. 2022, *MNRAS*, 513, 1801
 Larson, R. L., Finkelstein, S. L., Kocevski, D. D., et al. 2023, *arXiv e-prints*, arXiv:2303.08918
 López, S., D’Odorico, V., Ellison, S. L., et al. 2016, *A&A*, 594, A91
 Maiolino, R., Scholtz, J., Witstok, J., et al. 2023, *arXiv e-prints*, arXiv:2305.12492
 Matsuoka, Y., Onoue, M., Kashikawa, N., et al. 2019, *ApJ*, 872, L2
 Mazzucchelli, C., Bañados, E., Venemans, B. P., et al. 2017, *ApJ*, 849, 91
 Meyer, R. A., Bosman, S. E. I., & Ellis, R. S. 2019, *MNRAS*, 487, 3305
 Neeleman, M., Novak, M., Venemans, B. P., et al. 2021, *ApJ*, 911, 141
 Noll, S., Kausch, W., Barden, M., et al. 2012, *A&A*, 543, A92
 Oh, S. P. & Haiman, Z. 2002, *ApJ*, 569, 558
 Onoue, M., Kashikawa, N., Matsuoka, Y., et al. 2019, *ApJ*, 880, 77
 Padovani, P. 2017, *Nature Astronomy*, 1, 0194
 Pensabene, A., Carniani, S., Perna, M., et al. 2020, *A&A*, 637, A84
 Reed, S. L., Banerji, M., Becker, G. D., et al. 2019, *MNRAS*, 487, 1874
 Richards, G. T., Haiman, Z., Pindor, B., et al. 2006, *AJ*, 131, 49
 Richards, G. T., Kruczek, N. E., Gallagher, S. C., et al. 2011, *AJ*, 141, 167
 Sakurai, Y., Yoshida, N., Fujii, M. S., & Hirano, S. 2017, *MNRAS*, 472, 1677
 Schindler, J.-T., Farina, E. P., Bañados, E., et al. 2020, *ApJ*, 905, 51
 Selsing, J., Fynbo, J. P. U., Christensen, L., & Krogager, J.-K. 2016, *A&A*, 585, A87
 Shen, Y. & Kelly, B. C. 2012, *ApJ*, 746, 169
 Shen, Y., Wu, J., Jiang, L., et al. 2019, *ApJ*, 873, 35
 Trakhtenbrot, B. & Netzer, H. 2012, *MNRAS*, 427, 3081
 Valiante, R., Schneider, R., Volonteri, M., & Omukai, K. 2016, *MNRAS*, 457, 3356
 Vanden Berk, D. E., Richards, G. T., Bauer, A., et al. 2001, *AJ*, 122, 549
 Vernet, J., Dekker, H., D’Odorico, S., et al. 2011, *A&A*, 536, A105
 Vestergaard, M. & Osmer, P. S. 2009, *ApJ*, 699, 800
 Vestergaard, M. & Peterson, B. M. 2006, *ApJ*, 641, 689
 Vestergaard, M. & Wilkes, B. J. 2001, *ApJS*, 134, 1
 Volonteri, M. 2010, *A&A Rev.*, 18, 279
 Volonteri, M., Habouzit, M., & Colpi, M. 2021, *Nature Reviews Physics*, 3, 732
 Wang, F., Yang, J., Fan, X., et al. 2021, *ApJ*, 907, L1
 Willott, C. J., Delorme, P., Reylé, C., et al. 2010, *AJ*, 139, 906
 Wu, J., Shen, Y., Jiang, L., et al. 2022, *MNRAS*, 517, 2659
 Yang, J., Wang, F., Fan, X., et al. 2021, *ApJ*, 923, 262
 Yang, J., Wang, F., Fan, X., et al. 2023, *arXiv e-prints*, arXiv:2304.09888
 Yang, J., Wang, F., Fan, X., et al. 2020, *ApJ*, 897, L14